AIAA JOURNAL
Vol. 33, No. 11, November 1995

Shape Memory Ceramic Actuation of Adaptive Structures

Kamyar Ghandi* and Nesbitt W. Hagood†
Massachusetts Institute of Technology, Cambridge, Massachusetts 02139

Field-induced phase transitions in electroceramics with the advantages of large strain and shape memory are investigated as a mechanism for structural actuation. Several lanthanum and niobium doped lead zirconate stannate titanate compositions were manufactured and studied. The dependence of the material response on various factors relevant to structural actuation has been examined. Factors such as induced stress, actuation frequency, and temperature play an important role in the response of the material. A prototype adaptive structure using shape memory ceramic active materials has been constructed, tested, and used to validate model predictions.

Nomenclature

$\boldsymbol{A}$	= extensional stiffness matrix in classical laminate plate theory
$\boldsymbol{B}$	= coupling stiffness matrix in classical laminate plate theory
$\boldsymbol{c}$	= material stiffness matrix
c_{ij}	= stiffness matrix elements
c^a, c^s	= effective stiffness of actuator and structure
$\boldsymbol{D}$	= bending stiffness matrix in classical laminate plate theory
E	= electric field
E	= Young's modulus
$\boldsymbol{M}$	= resultant moments
$\boldsymbol{M}_e$	= induced resultant moments due to actuator
$\boldsymbol{N}$	= resultant loads
$\boldsymbol{N}_e$	= induced resultant loads due to actuator
$\boldsymbol{S}$	= in-plane strain vector (engineering notation)
$\boldsymbol{S}^0$	= in-plane strain vector along $z = 0$
S_{ij}	= components of the strain tensor
$\boldsymbol{s}$	= material compliance matrix
s_{ij}	= compliance matrix elements
$\boldsymbol{T}$	= in-plane stress vector
T_{ij}	= components of the stress tensor
t^a, t^s	= thickness of actuator and of structure
κ	= curvature vector
Λ	= free strain vector
ν	= Poisson's ratio
τ	= thickness ratio
ψ	= stiffness ratio

Introduction

PIEZOCERAMICS have been utilized in a variety of applications taking advantage of the electromechanical coupling of the material. They are utilized in manufacturing transducers such as strain gauges, pressure transducers, and accelerometers. They have also been used as actuators for control of dynamic structures and for damping of vibrations.[1] These actuators are ideal for many applications since they can be operated by electric fields, are compact, and can produce precise deformations. Unfortunately, conventional electroceramics such as piezoelectrics and electrostrictors have a small energy density, limiting their actuation capability. The strain levels of these materials are adequate for applications such as micropositioning devices and vibration control. However, other applications such as aeroelastic control and static shape control need higher actuator authority to be feasible. New materials are needed to achieve this goal.

A broad class of materials that show promise for such applications are electroceramics that undergo field-induced phase transitions. Field-induced phase transitions have been investigated by several authors.[2,3] Large strains have been observed to occur during the antiferroelectric (AFE) to ferroelectric (FE) phase transition in certain piezoceramics. Furthermore, certain classes of material, due to metastability of both phases, are capable of maintaining a residual strain even after the electric field has been switched off. Two families of materials displaying such behavior are the lead lanthanum zirconate stannate titanate (PLZST) family of ceramics studied by Cross[2] and the lead niobium zirconate stannate titanate (PNZST) family of ceramics studied by Oh et al.[3]

The study is motivated by two factors. First, strain levels as high as 0.6% have been reported to occur during the phase transition. Second, the use of shape memory in shape control has advantages such as simplifying the use of large number of actuators and reducing the number of amplifiers required. The feasibility of using the strain associated with phase transition in actuating adaptive structures is the primary focus of the present work. Thus, the materials have been studied with consideration given to factors such as temperature and structural stress, which affect the response of the material during a given application.

In addition to material characterization, small test structures motivated by adaptive optics applications have been constructed. Both theoretical predictions and experimental data on the response of the structures are presented.

Material Behavior

In ferroelectrics, an electric field can cause mechanical strain due to the polarization of the material (Fig. 1a). Unlike ferroelectrics, antiferroelectrics do not display any macroscopic polarization. Rather, they contain two sublattices that are spontaneously polarized in opposite directions. This leads to zero net polarization. As a result very little strain is achieved at low electric fields. If the composition of an antiferroelectric material is close to the ferroelectric phase boundary (Fig. 2), a phase transition from AFE to FE can be induced by the application of a large electric field. This phase transition, which is caused by the switching of the domain orientations, is accompanied by a lattice distortion leading to a net volume expansion in the material.[3] The isotropic expansion manifests itself as a sharp jump in the strain level of the material (Fig. 1b). Following the transition into the ferroelectric phase, the material displays anisotropic strains due to the reorientation of the ferroelectric domains. Longitudinal strain levels ranging from 0.08 to 0.6% have been reported for various compositions.[2,3] The compositions studied in the present work have shown strain levels of ~0.3%.

As the electric field is reduced, the material may either return to its original state or remain in the ferroelectric state (exhibiting shape memory), depending on the exact composition of the material. The ceramics lacking shape memory are only stable in the

Received June 20, 1994; revision received May 8, 1995; accepted for publication May 8, 1995.

*Graduate Research Assistant, Department of Aeronautics and Astronautics, Room 37-356.

†Associate Professor, Department of Aeronautics and Astronautics, Room 33-313. Member AIAA.

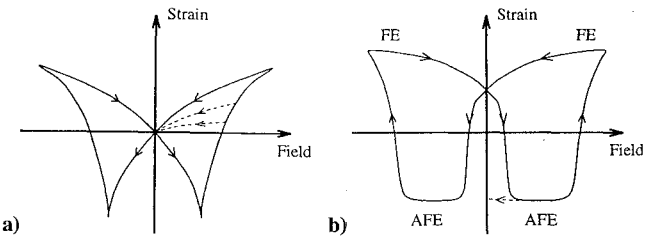

Fig. 1 Comparison of the longitudinal strains for ferroelectric and antiferroelectric materials: a) is ferroelectric and b) undergoes field-induced phase transition from antiferroelectric to ferroelectric and vice versa.

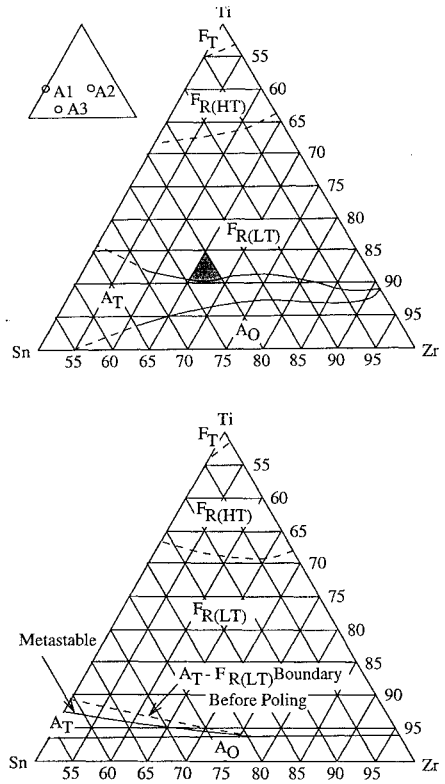

Fig. 2 Top: phase diagram for $Pb_{0.97}La_{0.02}(ZrTiSn)O_3$. The inset shows the compositions manufactured for this study. Bottom: phase diagram for $Pb_{0.99}Nb_{0.02}(ZrTiSn)O_3$.[4]

antiferroelectric state at zero field, whereas those with shape memory are metastable in either of the ferroelectric or the antiferroelectric states at zero field. If shape memory is present, a field in the opposite direction must be applied to induce the reverse transition and thus remove the residual strain.

Material Manufacturing

To evaluate the response of the various material compositions and to obtain sufficient data for modeling the material, several piezoceramic compositions were manufactured by the author in the Ceramic Processing Research Lab at the Massachusetts Institute of Technology. The compositions of the materials studied for this paper are listed in Table 1, and their location on the appropriate phase diagrams are shown in Fig. 2 (taken from Berlincourt[4]). Standard ceramic processing techniques were used in the manufacturing. Reagent grade oxides were mixed and ballmilled for 24 h. The powder was then sieved through a 45-μm mesh and calcined at 800°C for 10 h. The ballmilling and calcination steps were then repeated to ensure complete reaction of the powder and uniformity of composition. The powder was then pressed into 1-in.-diameter cylinders and isopressed to 40000 psi. Each cylinder was sintered in a PbO-rich atmosphere. The sintering schedule consisted of a 5-h-long ramp up to 1350°C, which was then maintained for 5 h, and a 5-h ramp down

Table 1 Compositions of the electroceramics for which data are presented

A1	$Pb_{0.97}La_{0.02}(Zr_{0.65}Ti_{0.115}Sn_{0.235})O_3$
A2	$Pb_{0.97}La_{0.02}(Zr_{0.67}Ti_{0.115}Sn_{0.215})O_3$
A3	$Pb_{0.97}La_{0.02}(Zr_{0.66}Ti_{0.105}Sn_{0.235})O_3$
B1[a]	$Pb_{0.99}Nb_{0.02}(Zr_{0.551}Ti_{0.0617}Sn_{0.3673})O_3$

[a]Supplied by Kenji Uchino at Pennsylvania State University.

to room temperature. The cylinders were then sliced into wafers using an ID saw [Staveley Sensors, Inc., East Hartford, CT, Tel: (203) 289-5428]. Each wafer was electroded using thermal evaporation of aluminum.

Material Characterization

A series of tests were performed on each composition, and typical results are presented. The accuracy of the data is discussed at the end of the section.

Free Strain Tests

The first series of tests were the measurement of transverse and longitudinal strains in the ceramic wafers, under an applied electric field. The experimental apparatus for obtaining simultaneous transverse and longitudinal measurements is shown in Fig. 3. An interferometric system was utilized to obtain the longitudinal displacement of the sample, while a strain guage provided transverse strain measurements. Characteristic field-strain curves for the A3 and B1 compositions are shown in Figs. 4 and 5. These curves correspond to the response while applying an electric field with a triangular waveform at 0.05 Hz. Compositions A1 and A2 displayed purely ferroelectric response (at 23°C) and are not shown. As expected for a ferroelectric material, the transverse strain curves were similar in shape to the longitudinal strain curve, but with opposite sign. Compositions A3 and B1 demonstrated antiferroelectric-ferroelectric switching. For electric fields limited to 2.2 kV/mm, longitudinal strains of approximately 2200 and 2700 $\mu\varepsilon$ were attained by A3 and B1, respectively, at room temperature. Note that the strains associated with both of these samples have the same sign in the longitudinal and transverse directions, indicating the phase transition is the dominant mechanism for creating strain.

It can be seen from the residual strain at zero field that both compositions A3 and B1 possess some shape memory. It should be noted that the transverse strain at zero field was as high as 75% of the peak strain. The longitudinal strain at zero field, however, was much lower than the peak value. This results from the combination of the anisotropic ferroelectric strain and the isotropic strain associated with the phase transition. This may be understood by considering the strains as the field is reduced from its maximum amplitude to zero. In the longitudinal direction, the strain due to the phase transition and the strain due to the ferroelectric coupling between field and strain contribute to each other. As the field is reduced, the drop in the ferroelectric portion of the strain causes a large decrease in the overall strain. In the transverse direction, the ferroelectric portion of the strain has the opposite sign. Thus, as the field is reduced, the strain actually increases (this is more evident in Fig. 10). In either direction, there is some drop in the strain that can be attributed to a fraction of the domains switching back to the antiferroelectric phase.

Temperature Tests

A series of tests were performed to characterize the behavior of the materials at different temperatures. The phase of the material is a function of its state. Along with the applied electric field, it is expected that quantities such as temperature and stress will be among the state variables. One can think of the phase boundary shifting due to a temperature change. Since the phase transition depends on the position of the specific material composition relative to the phase boundary, the behavior of the material depends on the operating temperature. This dependence has been investigated by conducting strain measurements at various temperatures in the range 0–45°C (Figs. 6–8).

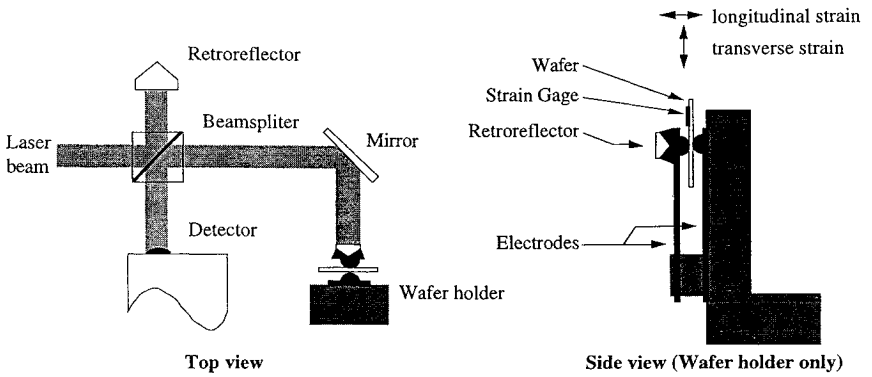

Fig. 3 Experimental setup used for simultaneous measurement of transverse and longitudinal strain. An interferometer provides longitudinal measurements, whereas a strain gauge provides transverse measurements.

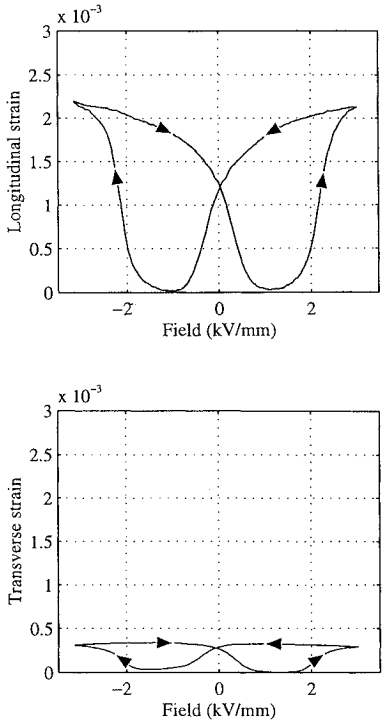

Fig. 4 Transverse and longitudinal field-strain curves for A3 ceramics.

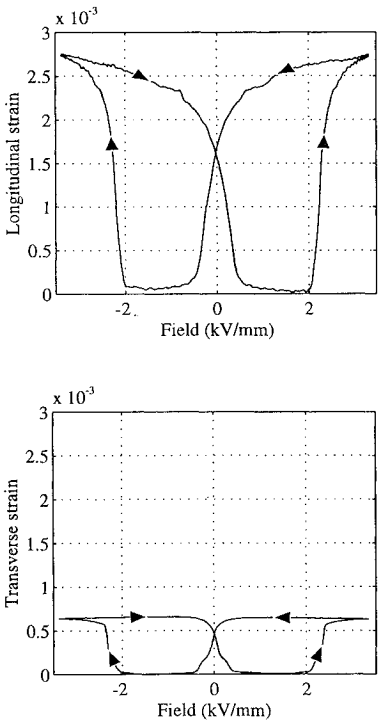

Fig. 5 Transverse and longitudinal field-strain curves for B1 ceramics.

The shape memory of the sample is seen more clearly in time domain tests. Figure 6b shows the strains in the A3 sample when applying an electric field with the time history shown in Fig. 6a. The magnitude of the positive voltage pulse was selected to force transition from AFE to FE. The negative pulse was made just large enough to cause the reverse transition. Of interest are the strain levels while the electric field is switched off. Several curves are shown corresponding to response at different temperatures. It is immediately obvious that over the temperature range considered the peak transverse strain increases with temperature. However, at higher temperatures the strain decays more rapidly.

Figure 7 shows these effects in more detail. The top curve is peak transverse strain induced by the electric field in Fig. 6a as a function of temperature. The bottom curve shows the minimum strain, which was attained during the application of the positive electric field. The middle curve in the figure is the residual strain after the field has been off for 4.5 s and is a measure of the amount of shape memory present. This residual strain peaks around 20°C. The rapid decay at higher temperatures can be attributed to an increase in the thermal vibrations of the lattice, which reduce the stability of the FE phase at zero field. Clearly, for shape memory applications, there is an optimal operating temperature where the magnitude of the residual strain is maximized. This optimal temperature can possibly be tailored for specific applications by making slight variations in

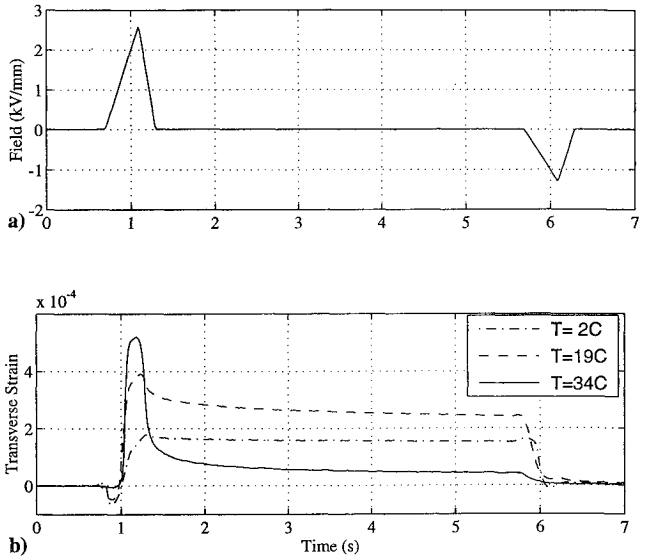

Fig. 6 Transverse strains in A3 sample arising from the application of the specified electric field at different temperatures.

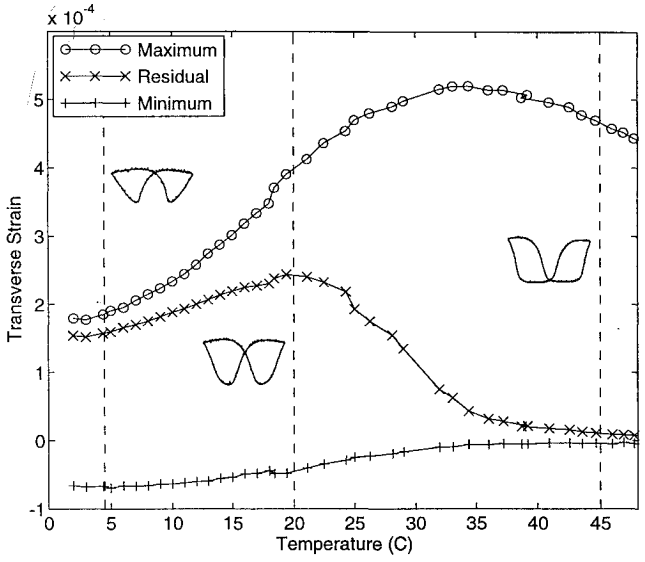

Fig. 7 Transverse strains of A3 sample during application of the electric field in Fig. 6a. The three curves correspond to peak strain, minimum strain, and the residual strain after 4.5 s. The insets show corresponding field-strain curves at selected temperatures.

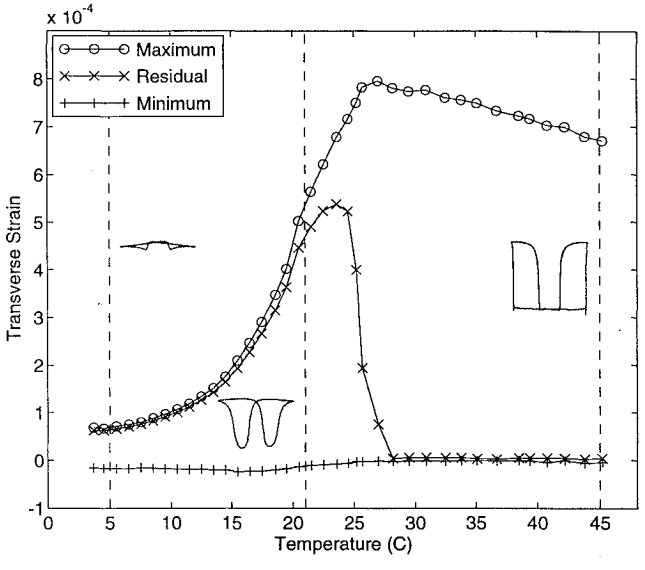

Fig. 8 Transverse strains of B1 sample during application of an electric field similar to Fig. 6a. The three curves correspond to peak strain, minimum strain, and the residual strain after 4.5 s. The insets show corresponding field-strain curves at selected temperatures.

the composition of the material. Figure 8 shows similar data for the B1 sample. This material exhibits more sensitivity to temperature as seen from the narrow peak in the residual strain curve. Its optimal operating temperature for shape memory is around 25°C.

The preceding results can be related to butterfly curves obtained at different temperatures. Field-strain curves at selected temperatures are superimposed on Figs. 7 and 8. At high temperatures both materials undergo the reverse transition (i.e., from FE to AFE) before the electric field has returned to zero and thus do not exhibit any shape memory. As the temperature was decreased, the onset of the reverse transition was delayed. This would be an advantage in terms of shape memory. Unfortunately, this was accompanied by a drop in the overall strain associated with the phase transition. At low enough temperatures, the phase transition in the B1 sample was inhibited all together, and the material appeared to behave as a ferroelectric. The strain associated with phase transition of the A3 samples decreased as the temperature was lowered. However, a phase transition was still observed even at the lower end of the temperature range studied. The higher temperature sensitivity of the niobium doped composition is possibly related to the fact that the material is antiferroelectric for a smaller range of compositions (see Fig. 2).

Table 2 Properties of the materials used in performing partially clamped wafer tests

	Material	E, GPa	ν	t, mil	ψ^a
b	Brass	105	0.35	2.5	0.23
c	Steel	190	0.30	4	0.62
d	Aluminium	70	0.35	20	1.24

[a] ψ [defined in Eq. (9)] values based on actuator stiffness $c^a = 116$ GPa, which was obtained experimentally.

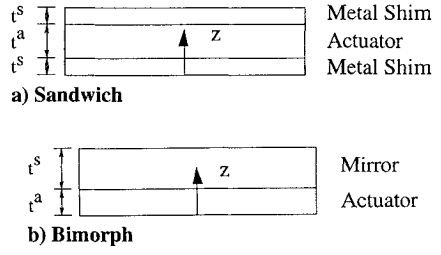

Fig. 9 Cross section of sandwich and bimorph test samples.

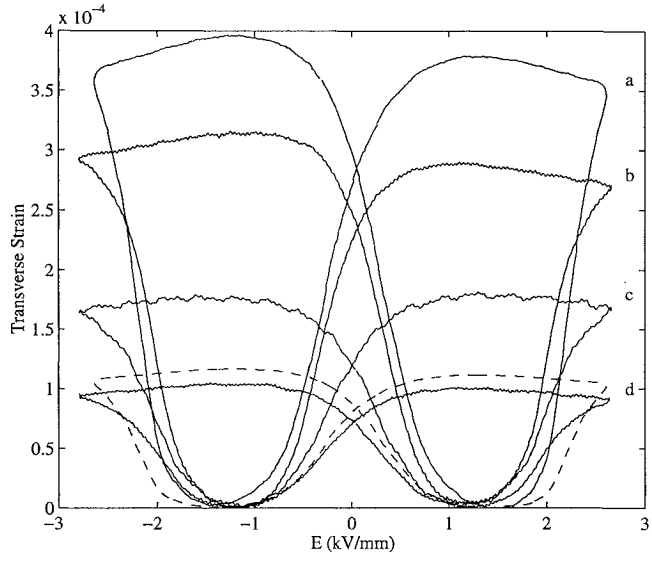

Fig. 10 Field-strain curves for partially clamped wafers: a) free wafer and b–d) wafer sandwiched between metal shims of increasing stiffness (see Table 2). The dashed curve shows predicted response corresponding to curve d.

Stress Tests

Another series of tests were aimed at determining the effect of stress on the sample. When electroceramics are used in structural applications, the elastic mechanical constraint imposed by the structure places stresses upon the material that will affect the observed strain. For example, it is necessary to ensure that structural stresses do not impede the phase transition in the actuator. Transverse strain measurements were performed on test articles consisting of metal shims bonded to both sides of the ceramic wafers (Fig. 9a). Figure 10 shows the observed transverse strains obtained under these partially clamped conditions. Curve a corresponds to a free wafer of the A3 sample. Curves b–d are the transverse strains produced by 15-mil-thick wafers sandwiched between metal shims with properties listed in Table 2. An immediate observation is that under the stiffness ratios examined phase transition was not impeded. It should be pointed out that there were cases where the shape memory was inhibited due to structural constraint. For example, an 11-mil-thick B1 wafer was partially clamped by bonding 40-mil-thick aluminum to each side. Figure 11 shows the transverse strain of this sample compared with one tested under free conditions. Note that due to the resulting stress in the sandwiched sample the phase transition was not accompanied by the large strain observed under free conditions and no shape memory is observed.

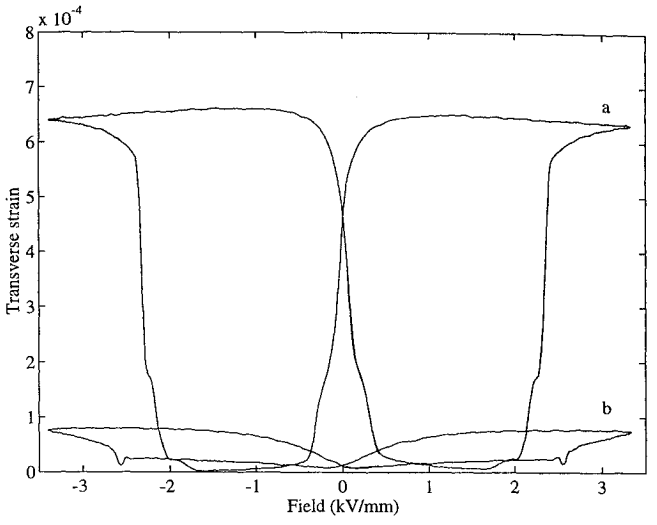

Fig. 11 Field-strain curves for wafers of sample B1: a) free and b) partially clamped.

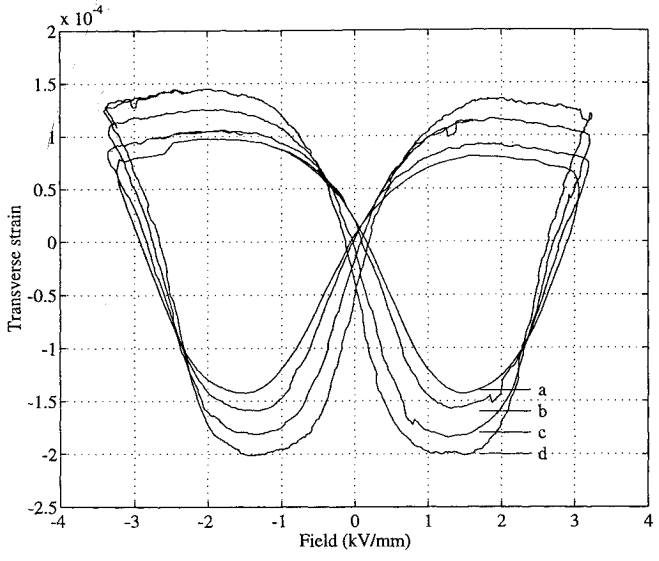

Fig. 12 Field-strain curves produced by a triangular electric field of amplitude 3.2 kV/mm at the following frequencies: a) 20 Hz, b) 2 Hz, c) 0.2 Hz, and d) 0.02 Hz.

The data from these clamped tests can be used to approximate the stiffness of the ceramic while it is in the ferroelectric phase. The method for modeling the system using classical laminated plate theory with induced stresses is described in the Appendix. The approach assumes symmetry of the problem in the x and y directions, leading to effective extensional stiffnesses for the structure c^s and the actuator c^a as defined by Eqs. (A12) and (A13). Solving the system for the transverse strain in the sandwich sample, Eq. (1) is obtained [see Eq. (A15) in the Appendix]:

$$S^0 = \frac{\Lambda}{1 + 2\psi} \tag{1}$$

where S^0 is the observed transverse strain of the structure and Λ is the transverse strain that the ceramic actuator would have experienced under free conditions. The variable ψ is the structure to actuator stiffness ratio in terms of the effective extensional stiffness and the thickness of each layer as defined by Eq. (A14).

With Eq. (1) a least-squares fit can be used to obtain an estimate of the effective structural stiffness c^a, defined in Eq. (A12). Multiple sandwich samples with different effective structure stiffnesses are used. For each sample, the ratio of Λ to S^0 at a given electric field level is measured and plotted against $2t^s c^s / t^a$. The slope of the best fit line then corresponds to $1/c^a$. This approach is based on the simplifying assumption that the stiffness does not change during phase transition. Although the validity of this assumption may be questioned, it is supported by the resulting fit with experimental data as seen in Fig. 10. The dashed curve in Fig. 10 shows the free strain data scaled according to Eq. (1) for the stiffness ratio corresponding to curve d of Fig. 10. Reasonable agreement between the two curves is observed. The assumption is also supported by experiments on a test mirror discussed in the next section. Predictions of deformations based on the stiffness measured in this fashion were found to show reasonable agreement with experimental measurements on the mirror.

Using the value of strains corresponding to an electric field of 1 kV/mm from Fig. 10, a value of 116 GPa was calculated for the effective stiffness $(c^*_{11} + c^*_{12})$ of A3 samples. Since all computations presented here use the effective stiffness, it was not necessary to decouple the c^*_{11} and c^*_{12} values. To decouple these parameters, one would need to assume/measure the Poisson's ratio of the material, ν.

Frequency Tests

The final series of tests involved obtaining strain data using electric fields with different frequencies. A triangular waveform was used. These tests were performed with wafers submerged in silicon oil to prevent arcing across the electrodes at high frequencies. The current required by the sample increases with frequency, since at higher frequencies the charge required for the phase transition must be supplied in a shorter period of time. Current limitations of the power supply restricted the maximum frequency of the tests to 10 Hz.

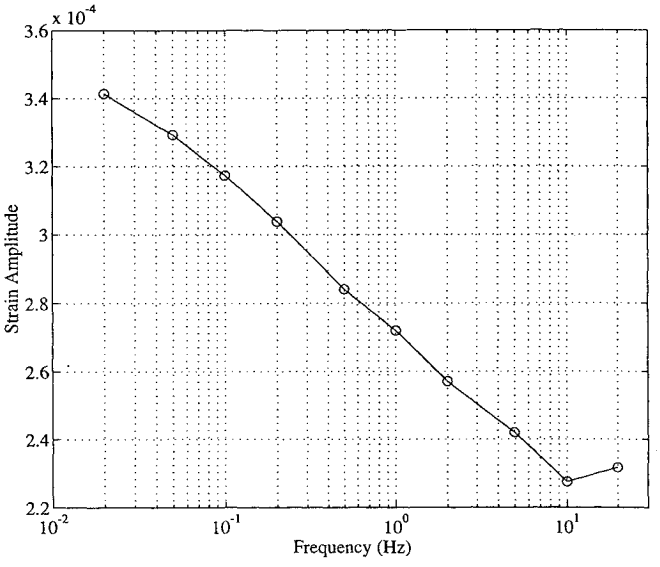

Fig. 13 Peak transverse strain in the ceramic wafer produced by a triangular electric field of amplitude 3.2 kV/mm at different frequencies.

The hysteresis of supplied current with voltage implies a power dissipation in the sample. This causes a rise in the sample temperature at higher frequencies. Since it is of interest to separate the effects of temperature and frequency, the oil temperature was adjusted during the experiment to maintain the wafer at approximately 26°C. Figure 12 shows some of the field-strain curves obtained from these tests. The strain amplitudes attained at each frequency are plotted in Fig. 13. The peak strain appears to decrease almost linearly with the log of frequency. The slope discontinuity at 10 Hz is caused by current saturation in the amplifier.

Experimental Accuracy

Various levels of accuracy are associated with the different measurements presented in this section. Transverse strains, measured using strain gauges, are accurate to $\pm 10\ \mu\varepsilon$. Longitudinal strains were obtained from interferometric displacement measurements. These measurements, although quite precise, are limited by vibrations to an accuracy of ± 8 nm. Sample thicknesses were measured to within ± 0.3 mil. These translate to longitudinal strain accuracy of $\pm 50\ \mu\varepsilon$.

The temperature measurements are accurate to ±1°C. For the high-frequency tests, however, a large temperature difference between the oil and the sample exist, and thus the measured temperature of 26°C may differ from the actual sample temperature by as much as 5°C.

By far the greatest concern is the accuracy of the compositions. The chemical compositions in Table 1 are based on starting oxide masses. All oxides used were 99.9+% pure, with the exception of ZrO_2 (99+% pure). Various steps in the processing introduce drifts in composition, with the most significant believed to be sintering, during which as much as 4% mass loss was observed. Composion accuracy can be greatly improved by refining the manufacturing process.

Structural Test Article

The knowledge gained from the material tests has been put into use in the design of a test article motivated by adaptive optics applications. An array of electroceramics bonded to the rear surface of a mirror may be used to correct deformations in the mirror. Although a great deal of work has been done in adaptive optics,[5,6] our goal is to demonstrate the benefits of using shape memory ceramics in such applications. There are several advantages associated with utilizing the strain associated with phase transition. The first is the large actuation capability attained from the high strain levels. The second is the residual strain at zero field. Rather than using a large array of amplifiers to actuate each actuator individually, a single amplifier can be used to program the actuators sequentially. This simplifies the requirements on the power supply and the driving circuitry.

Two prototype mirrors have been constructed, each with four piezoceramic wafers mounted on the rear (Fig. 14). The first mirror is actuated with PZT-5H (12.5-mil-thick) piezoceramic wafers and the second with A3 (15-mil-thick) wafers. A 0.5-mil-thick copper coated kapton sheet was bonded to the rear surface of a 7.5-cm-long, 1.25-cm-wide, and 0.1-cm-thick plane glass mirror, to provide a ground terminal for the ceramic wafers that were bonded on top. The ceramic wafers are 1.5 × 1.25 cm in dimension and are separated by 1 mm.

The same analysis used to calculate the stiffness of the ceramic from partial clamping data can be used to obtain a prediction of the mirror deflection. Equation (2), derived as Eq. (A16) in the Appendix, relates the strain S^0 and curvature κ of a bimorph (Fig. 9b) to the stiffness ratio of the mirror and actuator, their thicknesses, and the free strain of the actuator:

$$\kappa = -6\frac{\psi(1+\tau)\Lambda}{t^a(1+4\psi+6\psi\tau+4\psi\tau^2+\psi^2\tau^2)}$$
$$S^0 = \frac{(4\psi\tau^2+9\psi\tau+6\psi+1)\Lambda}{(1+4\psi+6\psi\tau+4\psi\tau^2+\psi^2\tau^2)} \quad (2)$$

The preceding equation is based on a plate model. Making the simplifying assumption that the curvature of the mirror is κ directly above the actuators and zero in between actuators, it can be integrated to obtain the profile of the mirror. Published stiffness values were used in the calculation of plane stress c^*_{11} and c^*_{12}, and thus c^a, for the PZT-5H wafers. The experimentally derived value was used for the A3 wafers. The relevant data for the model are listed in Table 3.

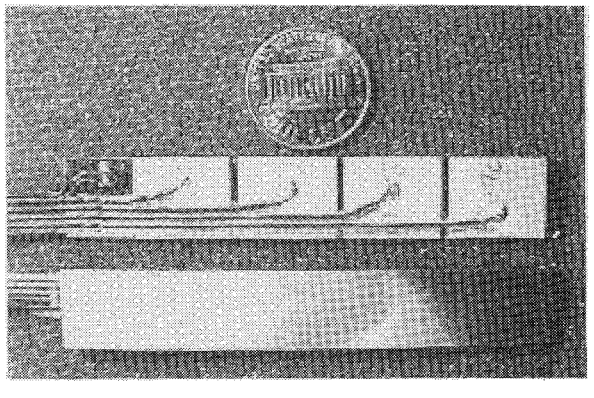

Fig. 14 Front and back views of the structural test article (a deformable mirror).

Table 3 Data used in mirror deflection predictions

	PZT-5H	A3		Glass
t^a, mm	0.317	0.381	t^s, mm	1.0
c^*_{11}, GPa	66.2	—	E, GPa	65.0
c^*_{12}, GPa	19.2	—	ν	0.16
c^a, GPa	85.4	116	c^s, GPa	77.4
Λ, $\mu\varepsilon$	220[a]	430[b]		

[a]Corresponding to $E = 0.6$ kV/mm (85% of coercive field).
[b]Corresponding to $E = 1$ kV/mm.

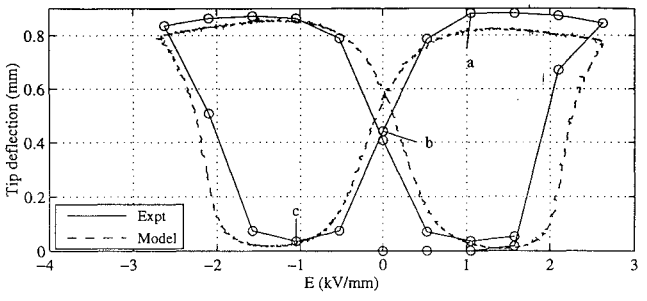

Fig. 15 Experimentally determined tip deflection of the shape memory ceramic actuated adaptive mirror at different applied field levels. The curve is compared with predicted tip deflections based on measured free strain.

The deformations were measured by directing multiple laser beams to points on the surface of the adaptive mirror. The reflected beams were observed on a screen placed 3 m from the mirror. Deformation of the mirror causes movement of the image points on the screen, which were recorded. Since the deflections of the mirror are quite small, only the slope of the mirror surface causes movement of the laser beams. Using a small angle approximation, it is a simple task to calculate the slope of the surface from the movement of the laser beams. The slope can then be integrated numerically to obtain the profile of the mirror.

Figure 15 shows the tip deflection of the A3 mirror during the quasistatic application of various field levels. All four wafers were actuated. The electric field was changed in 0.5 kV/mm steps at one minute intervals. At each new field level a 30-s settling time was allowed, and then deflections were measured. Also shown in the figure are the predicted tip deflections obtained by integrating the curvature from Eq. (A16) and using the experimentally measured free strain Λ and the free strain. There is fairly good agreement between the curves. There is a slight discrepancy in the location of the phase transition and the residual strain at zero field, which can be attributed to frequency response of the material. This results from using free strain values obtained at 0.01 Hz in the model. The 30-s settling time, during which some decay in the strain takes place, is not accounted for in the model.

Figure 16 shows the centerline profile of each mirror with all four wafers actuated, as measured experimentally and as predicted based on Eq. (A16). The PZT mirror deflection is shown for an applied electric field of 0.6 kV/mm, which is approximately 85% of the coercive field of the material. The A3 mirror deflection was measured at several field levels. It is shown at three field values that correspond to points labeled in Fig. 15. The good agreement of the experimentally measured deflection of the PZT mirror with the prediction serves to validate the calculations based on the experimental setup and the model. Good agreement is also seen for the A3 mirror in cases a and c. In case b, which corresponds to the electric field being zero, the model overpredicts the deflection. Again, this is caused by not accounting for the decay in the strain that occurs during the 30-s settling time.

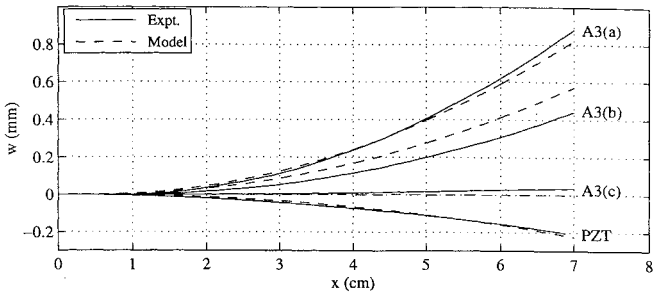

Fig. 16 Centerline deflection of the PZT-5H actuated mirror and the shape memory ceramic (A3) actuated mirror. The PZT mirror deflection is shown for an electric field of 0.6 kV/mm applied to all four wafers. The A3 mirror defection is shown for three field levels corresponding to those labeled in Fig. 15. For each case, the corresponding predicted shapes based on measured free strains are also shown.

Summary and Conclusions

Lanthanum and niobium doped piezoceramics, exhibiting antiferroelectric to ferroelectric phase transition, have been investigated for the purpose of utilizing their strain in structural actuation. Both compositions exhibit desired shape memory behavior. The niobium doped composition, although having slightly higher strains than the lanthanum composition, was found to be more sensitive to changes in temperature.

Numerous issues important in the use of such a material in applications have been examined. It was found that the observed strains are temperature dependent. There is a specific range of temperatures where the material is metastable in both the ferroelectric and antiferroelectric phases at zero field. In this region, field-induced phase transitions provide a mechanism for actuation, and shape memory is observed. If only the ferroelectric phase is stable, the material behaves like a conventional piezoelectric. This was the case with B1 material at temperatures slightly below room temperature. If only the antiferroelectric phase is stable at zero field, no shape memory will be observed. It was also observed that at higher temperatures the residual strain decays more quickly.

The importance of investigating strain under partially clamped conditions was presented. It is necessary to ensure that structural stress will not inhibit phase transition in the material as seen in the example with the B1 sample. In addition, clamped tests provide a means of calculating the stiffness of the ceramic. The brittle nature of ceramic wafers makes it difficult to use conventional tensile testing machines for this purpose. Based on the clamped tests, it was concluded that the stiffness of the material is relatively unchanged during the phase transition, making it possible to use an induced stress approach in modeling actuators utilizing this material.

A sample structure, motivated by adaptive optics, was constructed consisting of four shape memory ceramic wafers bonded to a mirror. The material data, along with a simple structural model based on plate theory, were used to successfully predict the behavior of a sample adaptive structure.

The results of the present study have demonstrated the feasibility of structural actuation using shape memory ceramics. The large strains associated with phase transition provide a great deal of actuation authority, and it was shown that the shape memory effect is present even under structural loads.

Numerous factors need to be considered in the design of such applications. Operating temperatures and the stiffness of the controlled structure have a significant effect on the phase transition. Furthermore, the response of the material decreases with frequency. The effect of each of these factors needs to be fully characterized to allow a successful application of these materials in adaptive structures.

Appendix: Laminate Modeling

Classical laminated plate theory (CLPT) is commonly used to model multilayer structures such as composite materials.[7] Structures such those in Fig. 9 can also be modeled using CLPT by using the concept of induced stress.[8] The approach is summarized in this section.

A plane stress assumption ($T_z = T_{yz} = T_{xz} = 0$) is made. Of interest are in-plane stresses and strains, which are related by

$$\boldsymbol{T} = \boldsymbol{c}^*\boldsymbol{S} \qquad \text{or} \qquad \boldsymbol{S} = \boldsymbol{s}^*\boldsymbol{T} \tag{A1}$$

where $\boldsymbol{S}$ is the 3×1 in-plane engineering strain vector, and $\boldsymbol{T}$ is the 3×1 in-plane stress vector:

$$\boldsymbol{S} = \begin{bmatrix} S_x \\ S_y \\ S_{xy} \end{bmatrix}, \qquad \boldsymbol{T} = \begin{bmatrix} T_x \\ T_y \\ T_{xy} \end{bmatrix} \tag{A2}$$

and $\boldsymbol{s}^*$ is the 3×3 compliance matrix, and $\boldsymbol{c}^*$ is the 3×3 stiffness matrix for the material. The symbol $(\cdot)^*$ is used to distinguish the reduced plane stress properties from their standard values in the 6×6 stiffness or compliance matrices. The reduced matrices can be written as

$$\boldsymbol{s}^* = \begin{bmatrix} s_{11} & s_{12} & 0 \\ s_{12} & s_{11} & 0 \\ 0 & 0 & s_{66} \end{bmatrix}, \qquad \boldsymbol{c}^* = \begin{bmatrix} c_{11}^* & c_{12}^* & 0 \\ c_{12}^* & c_{11}^* & 0 \\ 0 & 0 & c_{66}^* \end{bmatrix} = (\boldsymbol{s}^*)^{-1} \tag{A3}$$

Although the elements of the $\boldsymbol{s}^*$ matrix have the same values as the standard values in the full 6×6 matrix, the elements of the $\boldsymbol{c}^*$ matrix are different.

The structure is assumed to undergo Bernoulli–Euler bending. That is, a plane through the thickness of the structure will remain planar, such that the strain at any point can be written as

$$\boldsymbol{S} = \boldsymbol{S}^0 + \kappa z \tag{A4}$$

Placing relation (A4) into the stress-strain relation (A1), one can write the stress $\boldsymbol{T}$ as

$$\boldsymbol{T} = \boldsymbol{c}^*\boldsymbol{S} = \boldsymbol{c}^*(\boldsymbol{S}^0 + \kappa z) \tag{A5}$$

Proceeding with standard plate theory, resultant loads $\boldsymbol{N}$ and moments $\boldsymbol{M}$ in the plate are calculated by integrating the stress through the thickness of the test article:

$$\begin{aligned} \boldsymbol{N} &= \int \boldsymbol{S}\,\mathrm{d}z = \left(\int \boldsymbol{c}^*\,\mathrm{d}z\right)\boldsymbol{S}^0 + \left(\int \boldsymbol{c}^* z\,\mathrm{d}z\right)\kappa \\ \boldsymbol{M} &= \int \boldsymbol{S}z\,\mathrm{d}z = \left(\int \boldsymbol{c}^* z\,\mathrm{d}z\right)\boldsymbol{S}^0 + \left(\int \boldsymbol{c}^* z^2\,\mathrm{d}z\right)\kappa \end{aligned} \tag{A6}$$

The quantities in parenthesis are functions only of the geometry and the material properties and can be easily evaluated. Thus, the extensional stiffness $\boldsymbol{A}$, the coupling stiffness $\boldsymbol{B}$, and the bending stiffness $\boldsymbol{D}$ of the structure are defined to be

$$\boldsymbol{A} = \int \boldsymbol{c}^*\,\mathrm{d}z, \qquad \boldsymbol{B} = \int \boldsymbol{c}^* z\,\mathrm{d}z, \qquad \boldsymbol{D} = \int \boldsymbol{c}^* z^2\,\mathrm{d}z \tag{A7}$$

To satisfy equilibrium conditions, the structural loads and moments must balance the induced loads and moments caused by the actuator. The induced loads and moments are given by

$$\boldsymbol{N}_e = \int_a \boldsymbol{c}^*\,\mathrm{d}z\Lambda \qquad \boldsymbol{M}_e = \int_a \boldsymbol{c}^* z\,\mathrm{d}z\Lambda \tag{A8}$$

where $(\cdot)_e$ denotes electrically induced loads, and Λ is the vector of the actuator strains under free conditions. The integrals in Eq. (A8) are evaluated over the thickness of the active layers only. Equating the structural and induced loads and moments from Eqs. (A6) and (A8), the following relation is obtained:

$$\begin{bmatrix} \boldsymbol{A} & \boldsymbol{B} \\ \boldsymbol{B} & \boldsymbol{D} \end{bmatrix} \begin{bmatrix} \boldsymbol{S}^0 \\ \kappa \end{bmatrix} = \begin{bmatrix} \boldsymbol{N}_e \\ \boldsymbol{M}_e \end{bmatrix} \tag{A9}$$

Given the induced loads on the structure, Eq. (A9) can be solved for the strains and curvatures in system. If the structure and the loads

in the problem under consideration are symmetric in the x and y directions, the resulting strains will also be symmetric. Hence,

$$\kappa = \begin{bmatrix} \kappa_x \\ \kappa_y \\ \kappa_{xy} \end{bmatrix} = \begin{bmatrix} \kappa \\ \kappa \\ 0 \end{bmatrix} \qquad S^0 = \begin{bmatrix} S_x^0 \\ S_y^0 \\ S_{xy}^0 \end{bmatrix} = \begin{bmatrix} S^0 \\ S^0 \\ 0 \end{bmatrix}$$
$$\Lambda = \begin{bmatrix} \Lambda_x \\ \Lambda_y \\ \Lambda_{xy} \end{bmatrix} = \begin{bmatrix} \Lambda \\ \Lambda \\ 0 \end{bmatrix} \tag{A10}$$

By substituting Eq. (A10) into Eq. (A9) and collecting terms, one can simplify the system to

$$\begin{bmatrix} A & B \\ B & D \end{bmatrix} \begin{bmatrix} S^0 \\ \kappa \end{bmatrix} = \begin{bmatrix} N_e \\ M_e \end{bmatrix} \tag{A11}$$

The problem has been reduced to a one-dimensional system. The quantities A, B, D, N_e, and M_e are the effective values for the new system. They can be computed using definitions similar to Eqs. (A7) and (A8) by replacing the stiffness matrix c^* by the effective stiffness given by

$$c = c_{11}^* + c_{12}^* \tag{A12}$$

The integrals in Eqs. (A7) and (A8) can be evaluated in a piecewise manner over different layers. Superscripts s and a will be used to distinguish the properties of the structural layers and the active layers. Note that for the structural layers, which are isotropic, the effective stiffness (A12) can also be written in the form

$$c^s = E/(1 - \nu) \tag{A13}$$

The final expressions will be simplified by defining the nondimensional stiffness and thickness ratios as

$$\psi = t^s c^s / t^a c^a \qquad \tau = t^s / t^a \tag{A14}$$

Evaluating A, B, D, N_e, and M_e for the sandwich problem, and solving Eq. (A11) for the strain and curvature, one obtains

$$\kappa = 0 \qquad S^0 = \frac{\Lambda}{1 + 2\psi} \tag{A15}$$

Similarly, for the bimorph problem the equations yield

$$\kappa = -6\frac{\psi(1+\tau)\Lambda}{t^a(1 + 4\psi + 6\psi\tau + 4\psi\tau^2 + \psi^2\tau^2)}$$
$$S^0 = \frac{(4\psi\tau^2 + 9\psi\tau + 6\psi + 1)\Lambda}{(1 + 4\psi + 6\psi\tau + 4\psi\tau^2 + \psi^2\tau^2)} \tag{A16}$$

The free strain of the ceramic due to the applied electric field Λ determines the level of actuation. Depending on the geometry of interest, expression (A15) or (A16) can be used to compute the deformation of the structure. This approach may also be used to model laminates with more complicated arrangement of layers, by computing the extensional, coupling, and bending stiffnesses for the structure and using appropriate expressions for the induced loads and moments.

Acknowledgments

The research was funded by Jet Propulsion Laboratory Contract 959405 and monitored by Jim Fanson. We would like to thank Kenji Uchino of Pennsylvania State University for providing us with samples of niobium doped piezoceramics.

References

[1]Crawley, E. F., and DeLuis, J., "Use of Piezoelectric Actuators as Elements of Intelligent Structures," *AIAA Journal*, Vol. 25, No. 10, 1987, pp. 1373–1385.

[2]Cross, L. E., "Polarization Controlled Ferroelectric High Strain Actuators," *Journal of Intell. Mater. Syst. and Struct.*, Vol. 2, July 1991, pp. 241–260.

[3]Oh, K., Furuta, A., and Uchino, K., "Field Induced Strains in Antiferroelectrics," *IEEE Ultrasonics Symposium*, 1990, pp. 743–746.

[4]Berlincourt, D., "Transducers Using Forced Transitions Between Ferroelectric and Antiferroelectric States," *IEEE Transactions on Sonics and Ultrasonics*, Vol. SU-13, No. 116, 1966.

[5]Kuo, C. P., and Wada, B. K., "Composite Deformable Mirror," *Active Telescope Systems*, SPIE, Vol. 1114, 1989, pp. 495–505.

[6]Kuo, C. P., and Bruno, R., "Optimal Actuator Placement on an Active Reflector Using Modified Simulated Annealing Technique," *Proceedings of 1st Joint U.S./Japan Conference on Adaptive Structures*, 1981.

[7]Jones, R. M., *Mechanics of Composite Materials*, Hemisphere, New York, 1975, pp. 147–175.

[8]Crawley, E. F., and Lazarus, K. B., "Induced Strain Actuation of Isotropic and Anisotropic Plates," *AIAA Journal*, Vol. 23, No. 6, 1991, pp. 944–951.